Numerical and Experimental Investigation of the Dynamics of a U-Shaped Sloshing Tank to Increase the Performance of Wave Energy Converters

Journal of *Marine Science and Engineering*

MDPI

Article

Numerical and Experimental Investigation of the Dynamics of a U-Shaped Sloshing Tank to Increase the Performance of Wave Energy Converters

Marco Fontana [1], Giuseppe Giorgi [1,*], Massimiliano Accardi [1], Ermanno Giorcelli [1], Stefano Brizzolara [2] and Sergej Antonello Sirigu [1]

[1] Marine Offshore Renewable Energy Lab, Department of Mechanical and Aerospace Engineering, Politecnico di Torino, 10129 Turin, Italy; marco_fontana@polito.it (M.F.); ermanno.giorcelli@polito.it (E.G.); sergej.sirigu@polito.it (S.A.S.)

[2] Kevin T. Crofton Department of Aerospace and Ocean Engineering, Virginia Polytechnic Institute and State University, Blacksbur, VA 24060, USA; stebriz@vt.edu

* Correspondence: giuseppe.giorgi@polito.it

Abstract: In this investigation, a comprehensive study was conducted on a U-shaped sloshing tank, based on reversing the classical treatment of such devices as motion stabilizers and using them instead to improve the performance of wave energy converters. The modeling encompasses a comparative analysis between a linear model and Computational Fluid Dynamics (CFD) simulations. The validation of the CFD methodology was rigorously executed via a series of experimental tests, subsequently enhancing the linear model. The refined linear model demonstrates a notable alignment with rigorously verified results, thus establishing itself as a reliable tool for advanced research, indicating promise for various applications. Furthermore, this novelty is addressed by simulating the integration of a U-tank device with a pitch-based wave energy converter, displaying a broadening of the operational bandwidth and a substantial performance improvement, raising the pitch motion of the floater to about 850% in correspondence with the new secondary peak over extended periods, effectively addressing previously identified limitations. This achievement contributes to the system's practical relevance in marine energy conversion.

Keywords: sloshing tank; wave energy; dynamics; numerical modeling; CFD; experimental validation

Citation: Fontana, M.; Giorgi, G.; Accardi, M.; Giorcelli, E.; Brizzolara, S.; Sirigu, S.A. Numerical and Experimental Investigation of the Dynamics of a U-Shaped Sloshing Tank to Increase the Performance of Wave Energy Converters. *J. Mar. Sci. Eng.* **2023**, *11*, 2339. https://doi.org/10.3390/jmse11122339

Academic Editors: Elizaldo Domingues Dos Santos and Liércio André Isoldi

Received: 16 November 2023
Revised: 5 December 2023
Accepted: 6 December 2023
Published: 11 December 2023

1. Introduction

The historical origins of sloshing tanks are tied to the pioneering research efforts of William Froude, a distinguished British engineer and naval architect of the 19th century. Froude's seminal contributions to naval architecture have left an indelible mark on the discipline's evolution, establishing enduring principles still relevant today. At the heart of Froude's inquiries lay the central challenge of mitigating the intrinsic rolling motion encountered by ships when traversing tumultuous seas. Sloshing tanks emerged as a pivotal tool for examining and mitigating ship roll; indeed, they are also recognized under the appellation of Anti-Roll-Tank (ART). These tanks by Froude [1], strategically positioned within a ship's hull and filled with water, were engineered to counteract and reduce the amplitude of a ship's rolling motion, enhancing its stability. The water tank's free-surface effect lengthened the rolling motion period and reduced the ship's stability; consequently, the system was abandoned. Later, Frahm [2] understood the importance of placing the horizontal leg or cross duct of the U-shaped tube below the center of gravity of the ship to take advantage of the stabilizing component developed via the horizontal acceleration of water. Minorsky conceived the active counterpart of Frahm's passive tank [3]. A restoring moment was developed by transferring the water directly with a proper phase from one leg of the U-tube tank to the other at a high rate.

In the past few decades, the performance of anti-roll tanks has received considerable attention. Chadwick and Klotter [4] investigated the use of tanks for the US Navy. Van Den and Vugts [5] and Stigter [6] studied the performance of various types of anti-roll tanks for the Netherlands Ship Research Center. Field and Martin [7] evaluated the performance of passive U-tube and free-surface roll stabilization systems. Webster et al. [8] studied the performance of free-flooding anti-roll tanks during the significant upgrade of the USS Midway. Later, Lee and Vassalos [9] investigated the use of flow obstructions inside the tank. Recently, Abdel Gawad et al. [10] studied the performance of passive U-tube anti-roll tanks. They modeled the ship's motion using a single degree of freedom in roll motion. They presented a detailed parametric study on the effect of tank damping; mass; location, as relative to the ship's center of gravity (CG); and tuning. They found that a well-tuned, well-designed tank can effectively reduce the roll motion. The numerical model to study the fluid motion of a U-tube tank and its performance was developed first by Stigter [6] and then Lloyd [11], who introduced a simplified one-dimensional model to study the oscillation of a rolling U-tank based on the Euler momentum equation. He obtained a damped double pendulum differential equation in which most parameters are determined using the system's geometry, except for the damping parameter. Most of the studies have focused on the non-linear rolling motion of ships in different sea conditions. At the same time, little effort has gone into studying the fluid motion inside the tank and estimating the damping coefficient, as pointed out by Gawad et al. [10]. More studies about the flow inside U-tube tanks were carried out with the increased computational power. Zhong et al. [12] performed CFD (Computational Fluid Dynamics) 2D (2-dimensional) simulation with the Finite Element method, in which the Navier Stokes equations are solved using the Galerkin scheme. Van Daalen et al. [13] studied the performance of a U-tank by means of fully 3D (3-dimensional) CFD numerical simulations validated via the experimental results. Bhushnan et al. [14] proposed a method to estimate the damping coefficient from curve regression of a free decay test in 2D and 3D numerical simulation and stated that the damping is quadratic with the velocity and most of the head losses are due to the bends of the U-tube. Kerkvliet et al. [15] tested and validated a new CFD code ReFRESCO with the experimental results and demonstrated the CFD code's effectiveness in calculating the roll damping of a U-shaped ART.

The aforementioned literature is dedicated to investigating the stabilizing influence exerted by the U-tank device, primarily with the aim of addressing the rolling dynamics of ships. However, this current research endeavors to introduce a distinctive perspective. Rather than concentrating solely on its stabilizing role, the U-tank is posited as a dynamic tuning element to augment the performance of wave energy converters. While preceding studies have focused on the mechanical nuances of stabilizing vessels, this work seeks to broaden the application of the U-tank beyond its traditional usage, transforming it into an element for optimizing and tuning the operational characteristics of wave energy conversion systems. The goal of this work is to broaden the response of a floating body, achieving a secondary peak response in an inertia-based wave energy converter, a feat facilitated by characterizing U-tank and wave energy converter (WEC) systems as conventional dynamic systems. Such integration does not disrupt the architecture of the energy harnessing system and can be easily assisted by other systems and techniques to improve the performance, such as acting on the system and Power-Take-Off (PTO) control [16] or broadening the frequency band of oscillating WECs, such as acting on their parametric resonance [17].

For this very reason, modeling assumes paramount significance in this context, and the quest for the objective is highly contingent upon the precision of the model. Consequently, it was necessary to execute a validation process for the Computational Fluid Dynamics (CFD) model of the U-tank device via an experimental campaign. Subsequently, the refinement of a linear model capable of effecting the coupling with the floating body was undertaken. Here, the fluid motion inside the U-tube, also called U-tank, is investigated using 3D numerical simulation with the Volume of Fluid (VOF) method. First, the model is validated with the experimental results with particular attention to resonance conditions in regular

harmonic motion. The grid sensitivity and time resolution effect are investigated. Finally, the low-fidelity linear lumped parameter model is validated by means of the high-fidelity CFD model and the comparison in regular motion and irregular motion is shown.

The remainder of the paper is organized as follows. Section 2 introduces the numerical modeling, commencing with the linear lumped parameter model in Section 2.1, followed by an exposition on the fluid dynamic modeling of the U-tank device in Section 2.2, with particular emphasis on spatial and time convergence studies. The experimental setup is described in Section 3, and the results are exposed in Section 4. In particular, the result section enlights the regular motion outcomes (Section 4.1) at first, followed by the linear model tuning in Section 4.2, and then, the irregular motion results in Section 4.3. The validated and tuned model is coupled with the WEC in Section 5. Finally, Section 6 encapsulates the conclusions drawn from this manuscript.

2. Numerical Model, Verification, and Validation

2.1. U-Tank Lumped Parameter Model

In 1961, Lloyd [11] developed an analytical model based on the Euler momentum equation to evaluate the performance of an oscillating U-tank. The model is first described, then some corrections to the Lloyd model are adopted and explained.

The model is based on applying the Euler equation along the y-axis of the U-tank, as shown in the scheme in Figure 1, where the height H refers to the total height of the device h_r, which is called "Datum Level" and represents the equilibrium water level from the midline of the horizontal duct. The latter, referred to by the subscript d, has the height h_d and width equal to w_d. The vertical chambers, or reservoirs, have width w_r, and their distance between the two centerlines is w. The mounting distance, i.e., the distance between the midline of the horizontal axis and the rotation center, is r_d. The water motion inside the U-tank is defined by the water level z but, for the sake of symmetry, and especially to lighten the notation, it is more convenient to refer to the angle τ formed between the instantaneous level z and the Datum Level.

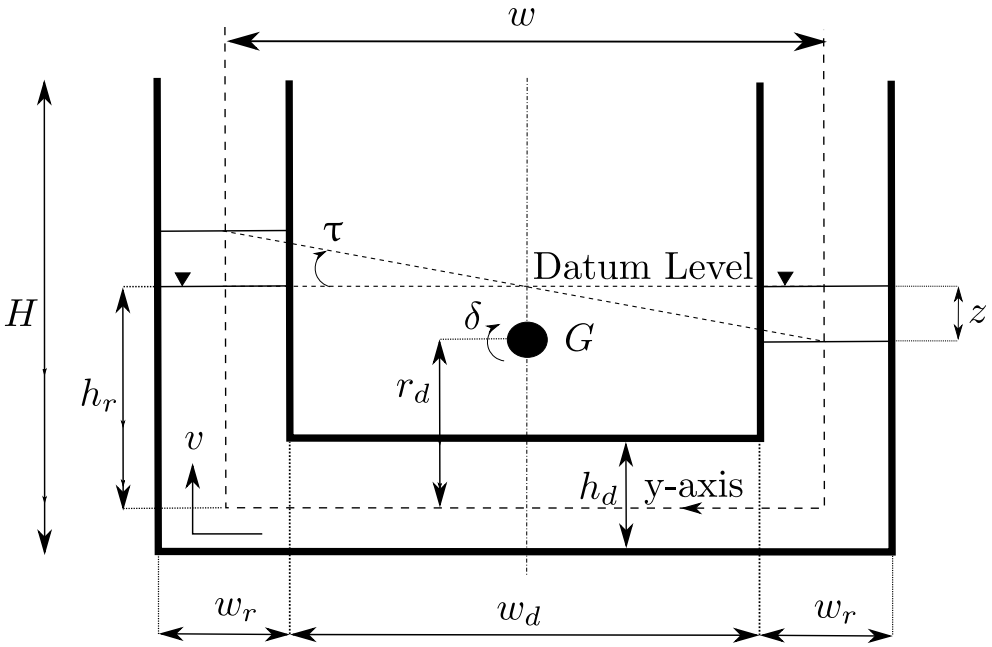

Figure 1. U-tank scheme and geometrical notations. The U-tank comprises a central horizontal duct and two vertical reservoirs in which the water reaches the Datum Level h_r at the equilibrium when the water angle τ is null. The center of rotation is G, in which the rotation δ is imposed.

The hypotheses of Lloyd's model are:

- The motion of the fluid is one dimensional and is expressed by the velocity v along the y-axis;
- Only pitch motion δ couples with the tank motion and it is applied in G, which is the center of oration of the U-tank device, and it will be the center of gravity of the WEC;
- The response of the tank due to a sinusoidal motion is also sinusoidal;
- The flow orthogonal to the y-axis, or cross flows are null.

Thus, Euler's equation can be written as:

$$\frac{\partial v}{\partial t} + v\frac{\partial v}{\partial y} = Y - \frac{1}{\rho}\frac{\partial p}{\partial y} \tag{1}$$

Following the Lloyd model description, the fluid velocity in the reservoirs, which have the same width w_r, is:

$$v = \frac{d}{dt}\left(\frac{z}{2}\right) = \frac{w}{2}\frac{d}{dt}\tan\tau \approx \frac{w}{2}\dot{\tau}, \tag{2}$$

where the last relation is based on the assumption that the water angle τ is small. Thus, for the continuity equation, the fluid velocity in any point of the tank can be expressed as:

$$v = \frac{w_r w}{2n}\dot{\tau} \tag{3}$$

where n is the U-tank width in the orthogonal direction of the y-axis. The external force per unit mass Y in Equation (1) is analyzed starting from the scheme in Figure 2 and it is composed by

- Gravity acceleration: $Y_g = -g\cos\alpha_1$
- External motion imposed by the pitch δ: $Y_\delta = -r\ddot{\delta}\sin\alpha_2$
- Frictional forces: $Y_q = qv/n$

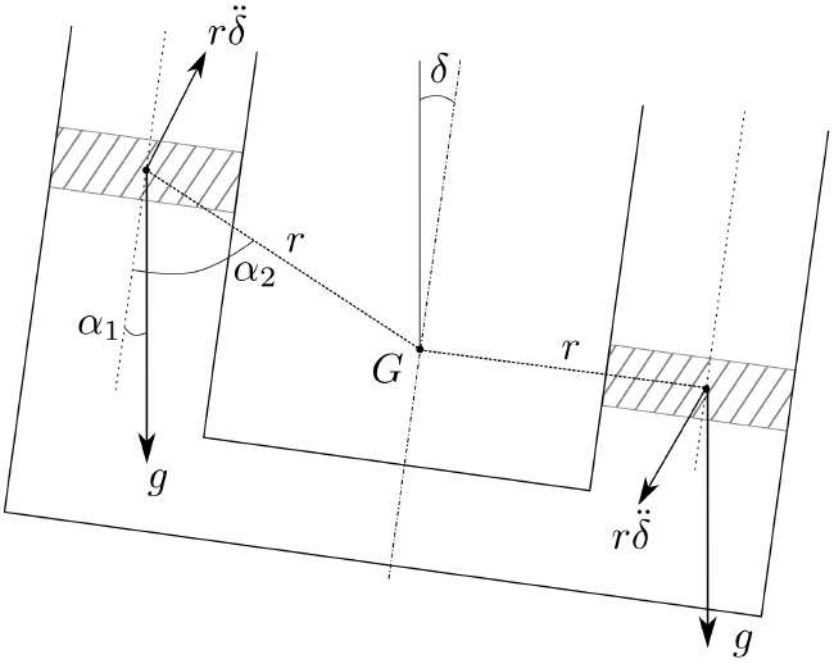

Figure 2. U-tank scheme with $\delta \neq 0$. The scheme is crucial to identify the external forces acting on the fluid within the U-tank with particular reference to the gravity acceleration and the angular acceleration imposed by the external motion δ, both represented by arrows.

Integrating the Equation (1) along the y-axis between the datum level of the reservoirs:

$$\frac{\rho w_r w I_1 \ddot{\tau}}{2} + \frac{\rho q w_r w I_2 \dot{\tau}}{2} + \rho g I_3 + \rho g I_4 = P_{\text{stern}} - P_{\text{bow}} \tag{4}$$

where the integration coefficients I_i are

$$I_1 = \int_{\text{tank}} \frac{dy}{n} = \frac{w}{h_d} + \frac{2h_r}{w_r}$$
$$I_2 = \int_{\text{tank}} \frac{dy}{n^2} = \frac{w}{h_d^2} + \frac{2h_r}{w_r^2}$$
$$I_3 = \int_{\text{tank}} \cos\alpha_1 dy = w\delta$$
$$I_4 = \int_{\text{tank}} r\sin\alpha_2 dy = w(r_d + h_r)$$

And the hydrostatic pressure difference between the two reservoirs on the right-hand side is

$$P_{\text{stern}} - P_{\text{bow}} = -\rho g w \tau$$

Equation (4) can be handled to obtain a typical canonical non-dimensional form by multiplying by the moment of area of the two reservoirs, considering the unit depth x_t:

$$Q_r = \frac{w w_r x_t}{2}$$

Finally, the lumped parameter model is obtained:

$$a_{\tau\tau}\ddot{\tau} + b_{\tau\tau}\dot{\tau} + c_{\tau\tau}\tau = -\left[a_{\tau 5}\ddot{\delta} + c_{\tau 5}\delta\right] \quad (5)$$

where:

- $a_{\tau\tau} = Q_t w_r I_1$
- $b_{\tau\tau} = Q_t q w_r I_2$
- $c_{\tau\tau} = Q_t g$
- $a_{\tau 5} = Q_t(r_d + h_r)$
- $c_{\tau 5} = Q_t g$
- $Q_t = \rho w Q_r$

Subscript 5 derives from the adopted naval notation in which δ is the pitch motion and the 5th degree of freedom. The frictional damping coefficient q can be modeled as a linear or non-linear coefficient (usually proportional to the velocity squared [18]); the different way to model this coefficient is beyond the purpose of this work. In this paper, only the linear damping coefficient will be used and estimated using the CFD free-decay test. The inertial coefficient will differ from the expression presented in Equation (5), mainly due to the different shapes of the corners concerning the Lloyd rectangular model. Employing experimental and CFD results, the terms $a_{\tau\tau}$ and $b_{\tau\tau}$ of the model will be tuned in Section 4.2 to ensure a good prediction of the results.

2.2. Fluid Dynamics Model

The CFD simulations were carried out using the commercial software STAR-CCM+ by Siemens [19].

The considered layout, in which the U-tank is open to the atmosphere, allows for the description of the system via the incompressible two-phase flow using the Navier–Stokes equations in a conservative form, expressing the conservation of the mass, moment, and the volume fraction of the primary phase. In general, it can be written as

$$\begin{cases} \dfrac{\partial\rho}{\partial t} + \nabla\cdot(\rho\mathbf{v}) = 0 & (6) \\ \dfrac{\partial\rho\mathbf{v}}{\partial t} + \nabla\cdot(\rho\mathbf{v}\mathbf{v}) = -\nabla p + \mu\nabla^2\mathbf{v} + \rho\mathbf{g} & (7) \\ \dfrac{\partial\alpha_i}{\partial t} + \nabla\cdot(\alpha_i\mathbf{v}) = 0 & (8) \end{cases}$$

In which the common notation of fluid dynamics is used:

- $\mathbf{v}$ is the velocity field;
- ρ is the fluid density as the weighted average of the two phases as described below;
- p is the pressure field;
- $\mathbf{g}$ is the gravity acceleration;
- α_i is the volume fraction of the i-th phase.

Two fluid phases, water and air, are contained within the U-tank device. For each cell, the following modeling is adopted:

$$\begin{cases} \alpha_2 & = 1 - \alpha_1 \\ \rho & = \alpha_1\rho_1 + \alpha_2\rho_2 = (\rho_1 - \rho_2)\alpha_1 + \rho_2 \end{cases} \tag{9}$$

The primary phase, with subscript "1", is the water phase. At the interface, the two phases share the same velocity (no-slip condition) and the pressure is set at atmospheric value. To describe the turbulent phenomena, the Reynolds-Averaged-Navier-Stokes (RANS) model is used whereby an instantaneous quantity ϕ is decomposed in its time-averaged and fluctuation quantities:

$$\phi = \bar{\phi} + \phi' \tag{10}$$

Hence, the continuity and momentum conservation in Equations (6) and (7) became:

$$\begin{cases} \dfrac{\partial \rho}{\partial t} + \nabla \cdot (\rho \bar{\mathbf{v}}) = 0 \\ \dfrac{\partial \rho \bar{\mathbf{v}}}{\partial t} + \nabla \cdot (\rho \bar{\mathbf{v}} \bar{\mathbf{v}}) = -\nabla \bar{p} + \nabla \cdot (\mu \nabla \bar{\mathbf{v}} - \mathbf{R}) + \rho \mathbf{g} \end{cases} \tag{11}$$

The new term $\mathbf{R} = \rho \overline{v_i' v_j'}$ is the Reynolds stress tensor that allows for the turbulence model to be used, with the drawback of increasing the system's unknowns. To close the set of partial differential equations in (11), the Realizable κ–ε model is used, where κ is the kinetic turbulent energy and ε is the turbulent dissipation rate. The *realizable* model differs from the standard since a new transport equation for the turbulent dissipation rate ε is provided from the vorticity fluctuation transport equation, and the eddy viscosity μ_t is assumed to be a function of the mean rate of the strain tensor and the mean flow. This procedure lets the model satisfy certain mathematical constraints on the normal stresses consistent with the physics of turbulence (realizability) [19,20]. Also, the dimensionless wall distance, commonly referred to as $y+$, is modeled with blended functions because of the wide variations during the simulation.

The other main models used are listed below:

- Volume of Fraction with High-Resolution Interface Capturing scheme (HRIC) and second-order convection;
- Second-order temporal discretization;
- Segregated Flow, in which the equations are solved one by one for a certain variable for all cells;
- Second-order upwind convection;
- Gradient method: Hybrid Gauss-LSQ;
- Limiter method: Venkatakrishnan.

2.3. Test Case

The U-tank device's scaled model is shown in Figure 3 and the main geometrical features are shown in Table 1. The CFD simulations are performed by considering half of the model via the symmetry in the x-z plane, allowing for the domain to be halved as well as the computational effort regarding spatial discretization. The only degree of freedom (DoF) is the rotation around the y-axis and it is imposed in the center of rotation (CoR) as

shown in Figure 3. The imposed rotation is defined in terms of harmonic angular velocity as follows:

$$\dot{\delta} = A\omega\cos(\omega t) \tag{12}$$

In which

- The motion amplitude is $A = 2\,\text{deg}\ (0.0349\ \text{rad})$;
- The angular frequency ω is defined from the period T.

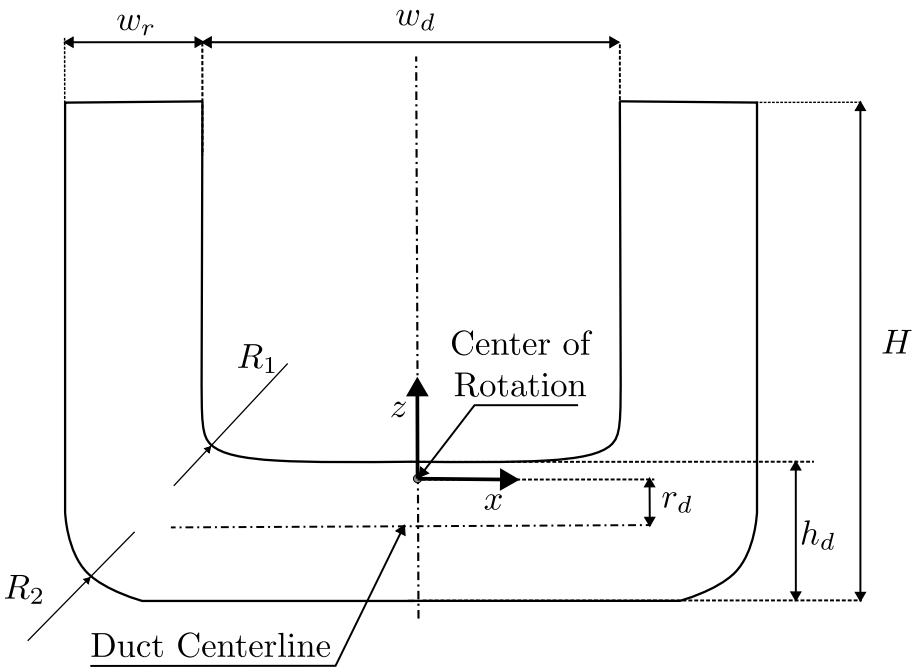

Figure 3. U-tank geometry of the test case of the CFD numerical simulations.

Table 1. U-tank test case geometrical characteristics.

Size	Symbol	Value	Unit
CoR Distance from duct centerline	r_d	63	mm
Duct Height	h_d	170	mm
Duct Width	w_d	514	mm
Reservoir Width	w_r	170	mm
Model Height	H	610	mm
Model Depth	x_t	100	mm
Inner Fillet Radius	R_1	65	mm
Outer Fillet Radius	R_2	115	mm
Water (Datum) Level	h_r	235	mm

The boundary conditions of the CFD simulation are shown in Figure 4 and defined as follows:

- Stagnation Inlet at the top of the reservoirs:
  - Static pressure is obtained using the Bernoulli equation as follows:

$$p_s = p_t - 1/2\rho|\mathbf{v}|^2$$

  - Velocity magnitude is extrapolated from the interior domain and the direction is normal to the boundary such that $v = |v^{\text{ext}}| \cdot n$, in which n is the inward-pointing normal vector to the surface.
- Symmetry condition at $y = 0$:

  - No fluxes through the surface due to Lloyd's assumption of null gradients in the n direction ($\partial/\partial n = 0$)
  - The face value of velocity is computed by extrapolating (superscript "ext") the velocity in the adjacent cell using reconstruction gradients and subtracting the normal velocity:

$$\mathbf{v} = \mathbf{v}^{\text{ext}} - (\mathbf{v}^{\text{ext}} \cdot \mathbf{n}) \cdot \mathbf{n}$$

- All the other boundaries are walls with a no-slip condition; thus, the relative velocity of the fluid is zero with respect to the wall.

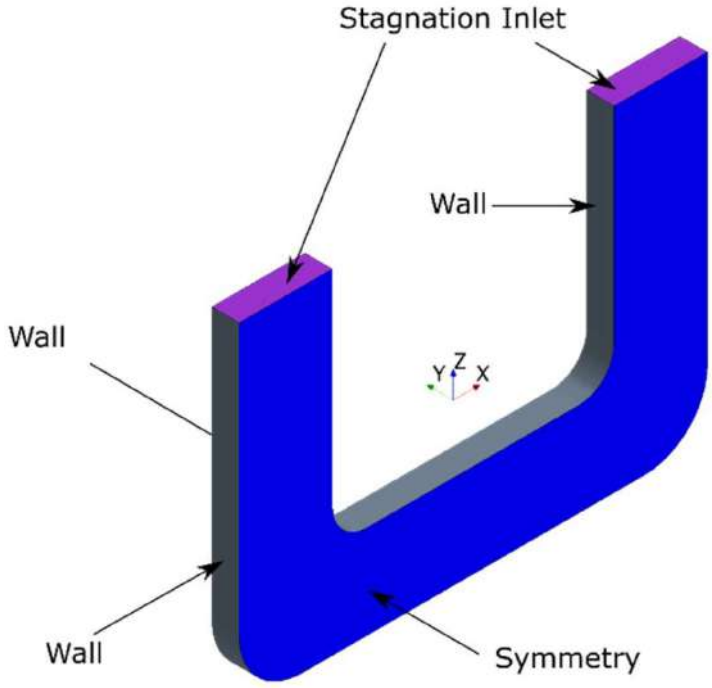

Figure 4. U-tank CFD test case Boundary Conditions. The blue face is a symmetry plane, the purple faces are stagnation inlet, and the other faces are no-slip walls.

The domain is discretized by a structured scheme in hexahedral cells, trimmed near the surfaces. The grid is refined in the two reservoirs to capture both the free surface straddling the water and the air phases correctly, thus keeping the model's accuracy. Also, a grid refinement is adopted at the elbows, as shown in Figure 5.

In order to correctly perform the grid convergence study with respect to the experimental tests of the following section, Section 3, all the mesh geometrical dimensional quantities are defined as percentages of the base size. The mesh setup is in terms of the cell's surface, corresponding to the base size $BS = 1$ m and discretization of the boundary layer, or prism layer, which is shown in the following table, Table 2. The boundary layer is modeled by imposing the size of the first wall cell, with growth toward the domain cells by a geometric progression of 30%. The goal is to fall back into the logarithmic zone of the boundary layer by reaching a value of $y+ = 40$ in the water-wet surface. In the following two sections of this paper, Sections 3.1.1 and 3.1.2, the convergence analysis is conducted by imposing the regular harmonic motion $\dot{\delta}$ defined above with a period of $T = 1.4$ s. The dependence study retains the ratio between the mesh base size and the time-step constant to keep the Courant number among the different cases.

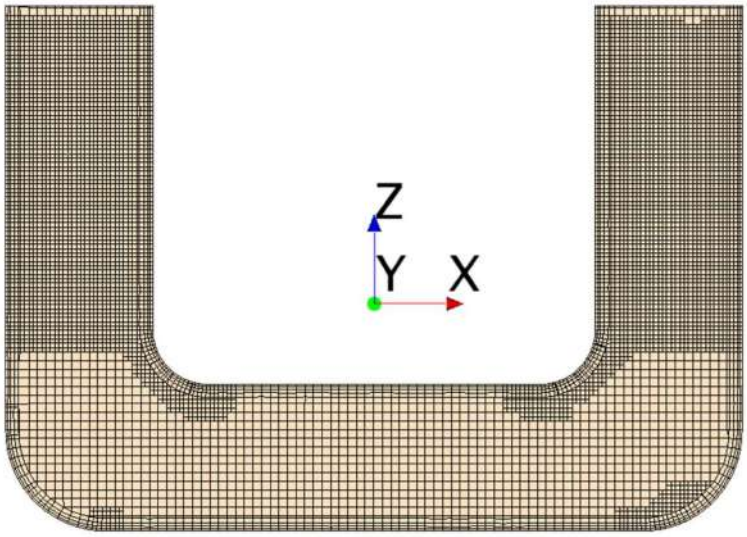

Figure 5. Side view of the mesh grid.

Table 2. U-tank mesh setup.

Size	Value	Unit
Surface size	10	mm
Surface size in the reservoirs	5	mm
Minimum Surface size	2.5	mm
Prism layer total thickness	15	mm
Number of prism layers	4	-
Prism layer stretching factor	1.3	-
Average $y+$	40	-

3. Experimental Tests

The validation process in the scope of this work is carried out based on an experimental campaign conducted with a 3-DoF platform called the Heave-Roll-Pitch (HPR) platform. The HPR device is electro-actuated with the following working limits:

- Roll and Pitch: ± 25 deg
- Heave: ± 300 mm

A digital signal processor, in which a Matlab/Simulink 2017b® code is compiled, allows for the platform's control. The rotational degree of freedom imposed is the previously defined δ and is represented by a sinusoidal profile according to Equation (12).

The U-tank scaled device is realized with transparent PVC panels to allow us to both inspect the fluid motion and follow the trajectory of the water level using infrared reflecting markers using a motion capture (MoCap) acquisition system by Qualisys® (Göteborg, Sweden). The system allows us to follow the markers' trajectories via Qualisys Track Manager (QTM), which were sampled with a frame rate of 100 Hz. The markers are fixed upon light floaters, whose weight can be neglected, to track the water level within each reservoir. The floating polystyrene panels on which the markers are installed eliminate the phenomenon of secondary sloshing, but this is negligible in the regime of small oscillations. The rear panel is realized with non-reflecting dark PVC to capture the marker via an infrared acquisition system. The U-tank scaled model and its installation on the motion platform through mounting brackets are shown in Figure 6.

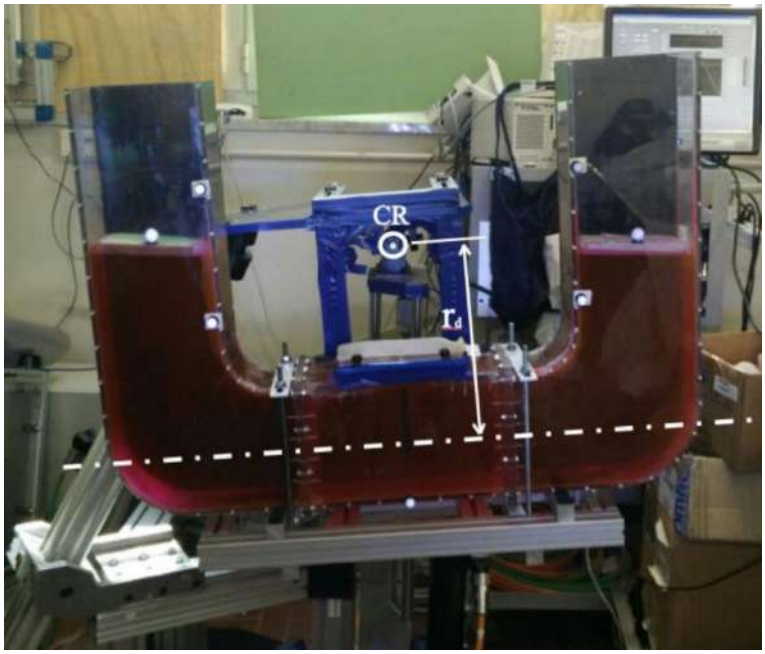

Figure 6. U-tank scaled device installed on the motion platform. The scheme includes the Centre of Rotation (CR) and the mounting size r_d. The white dots represent the reflecting markers, whose two couples are fixed on the inner sides of the reservoirs, one on the bottom of the central duct, and two are installed on the light floaters.

3.1. Convergence Analysis

Once the experimental campaign is settled, the first step is to perform spatial and temporal convergence analysis of the CFD simulations based on the asymptoticity of the discretization and the comparison with the experimental outcomes. In particular, it was chosen to assess regular angular motions by means of the electro-actuated platform with a sinusoidal signal of amplitude A = 2 deg and by varying the period between 1.1 and 2 s, as shown in Figure 7.

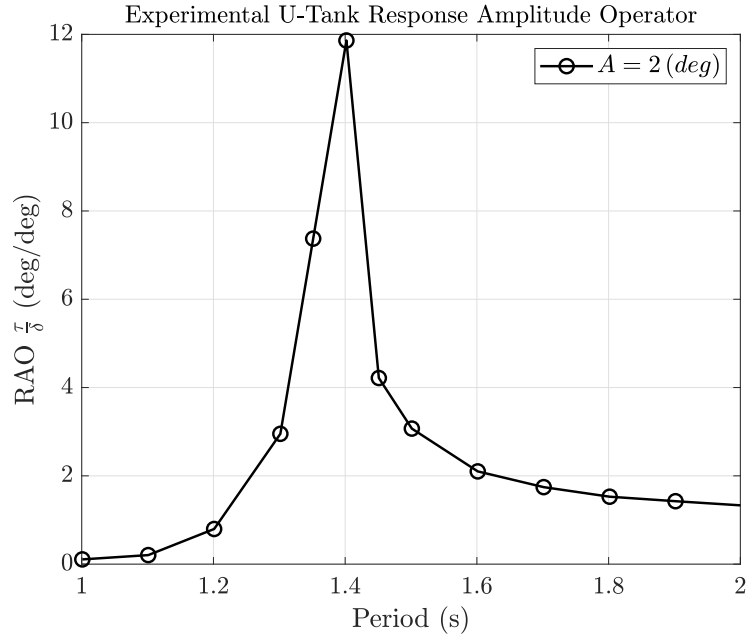

Figure 7. Response Amplitude Operator of the water angle τ with respect to the input amplitude A.

The comparison with CFD simulations is made at the resonance condition of the system, which is at 1.4 s. Both the mesh and time-step analysis are compared to the water level oscillation amplitude measured by means of the motion capture system.

3.1.1. Grid Convergence Study

The spatial discretization convergence is performed by varying the base size as shown in Table 3, and so the grid count and the density change accordingly. The results are compared, excluding the initial transient, specifically in the time range of 70.7–98.7 s. For example, the water level over time of the unitary base size is shown in Figure 8.

Table 3. U-tank mesh setup and grid convergence analysis.

ID	Base Size (m)	Cells	Cells per cm^3	Water Level Oscillation Amplitude (m)
Very Coarse	2	25,824	1.775	0.1241
Coarse	$\sqrt{2}$	49,324	3.391	0.1318
Medium	1	98,058	6.741	0.1393
Fine	0.5	552,079	37.95	0.1456
Very Fine	$0.5/\sqrt{2}$	1,436,525	98.76	0.1463

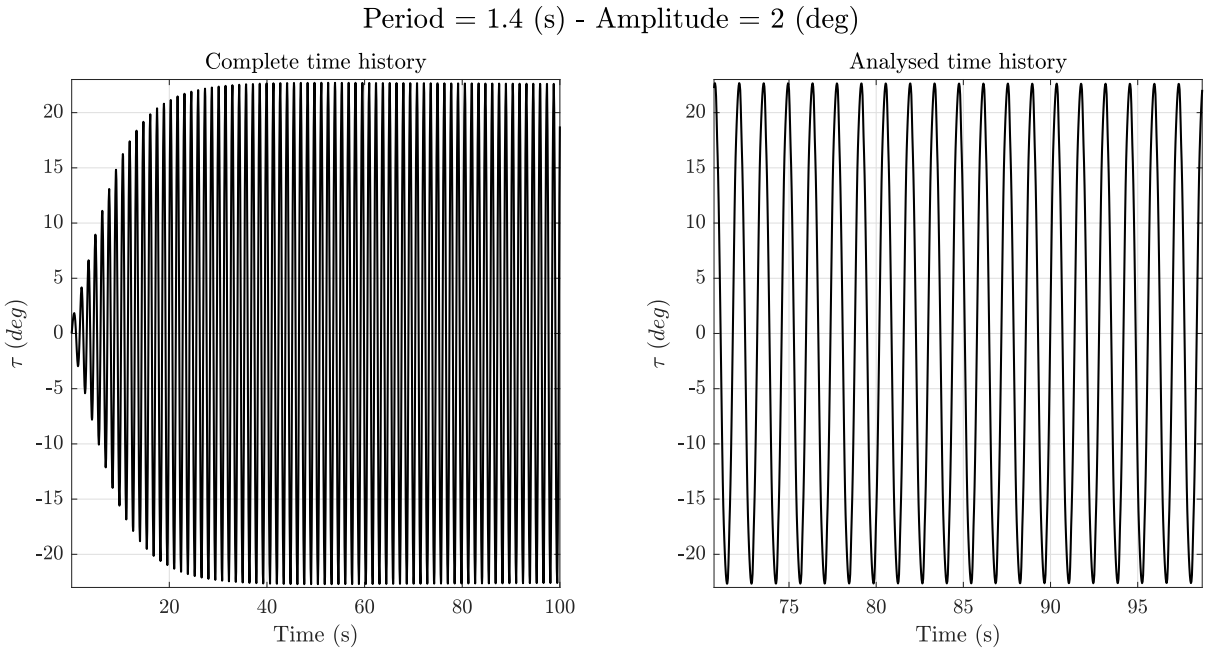

Figure 8. Time history of the water level signal of the unitary base-size CFD simulation on the left reservoir (**left**) and the portion of the analyzed signal (**right**).

The grid convergence study is illustrated in Figure 9 with the monotone curve of the water oscillation amplitude and the number of cells per cm^3. The first three values of the corresponding base size show a fast improvement in accuracy because the coarsest mesh is not fine enough to capture the phenomena correctly. Conversely, the last three values show an asymptotic behavior within a reasonable relative error compared with the experimental result as less than 10%, as shown in the blue y-axis on the right of the plot in Figure 9.

The grid size also affects the capability of capturing the interface between phases and the secondary waves at the upper elbows, as illustrated in Figure 10 for three different mesh cases. The Very Fine mesh case can capture the secondary wave with a good resolution, while the Medium case appears very smooth due to the cells' size. It also highlighted the capability of the fine cases in Figure 10b,c to capture the spray zones close to the free-surface interface (which is more evident in the left reservoir), which is a more realistic behavior of

the sloshing phenomenon. Nevertheless, this additional aspect is beyond the scope of this work, and the Medium case keeps a good accuracy with respect to the computational effort.

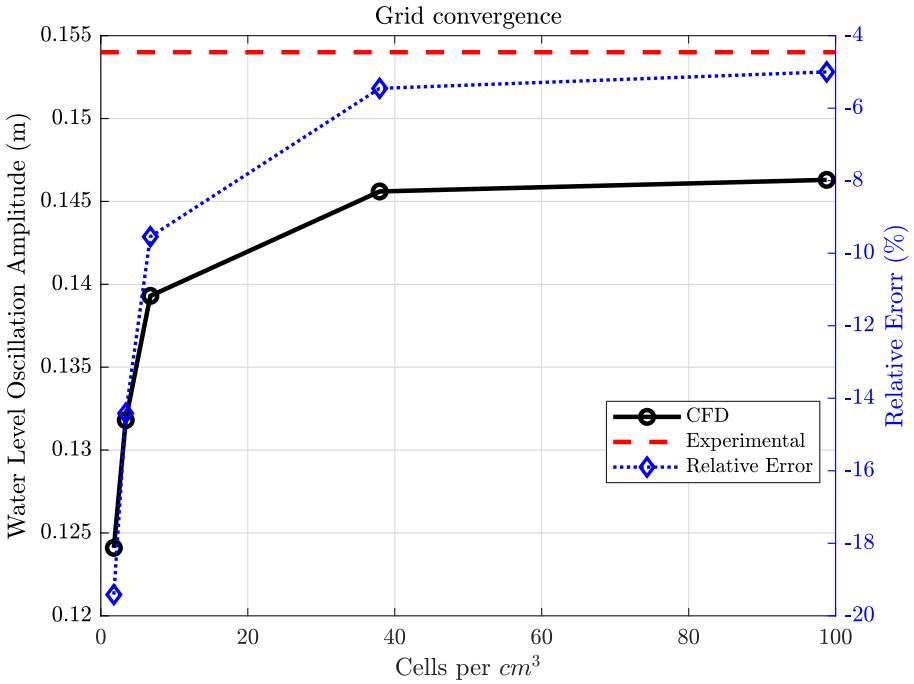

Figure 9. Grid convergence study results as the cells per cm^3 vary from the very coarse setup to the finer. The left axis in black refers to the absolute values of the water level amplitude (in continuous black line), and the right one in blue refers to the relative error (blue dotted line) with respect to the experimental result (dashed grey line).

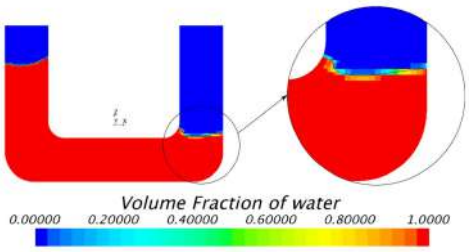

(**a**) Medium grid

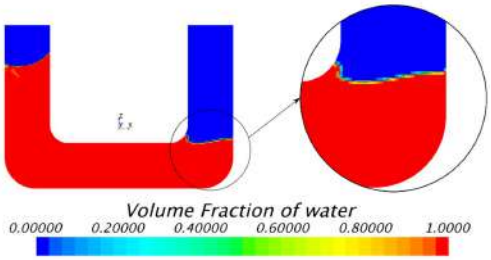

(**b**) Fine grid

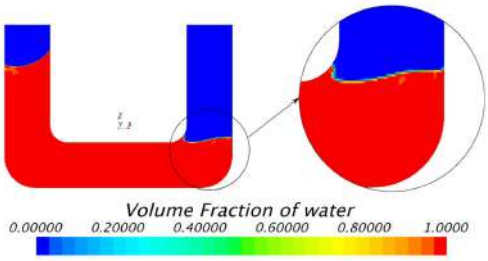

(**c**) Very fine grid

Figure 10. Volume fraction of water visualization at $t = 71.4$ s for three different cases in Table 3: (**a**) Medium grid with Base Size = 1 m, (**b**) Fine grid with Base Size = 0.5 m, and (**c**) Very Fine grid with Base Size = 0.35 m.

3.1.2. Time-Step Convergence Study

The time-step size plays a crucial role in capturing the sloshing phenomenon. In this study, the mesh case is set to Medium, the time step is gradually reduced, and the oscillation amplitude of the water level is computed and reported in Table 4. The curve in Figure 11 does not show an asymptotic convergence. Nevertheless, it is worth noting that all the considered time steps lead to a relative error within ±5%.

Table 4. Time-step convergence data compared to the water level oscillation amplitude.

Time Step (ms)	Water Level Oscillation Amplitude (m)
0.100	0.1557
0.167	0.1544
0.250	0.1526
0.500	0.1477

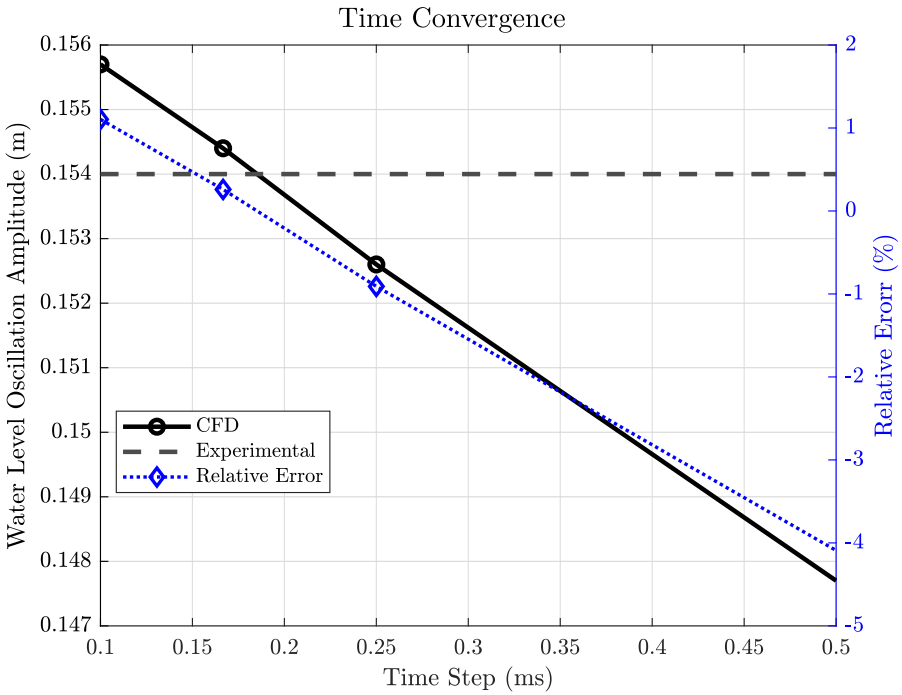

Figure 11. Time convergence study of water level oscillation amplitude versus time-step and relative error with respect to experimental data.

3.2. Mesh and Time-Step Choice

In order to retain an affordable computational effort and an acceptable error concerning the experimental results, the adopted setup is the time step $dt = 0.5$ ms and the Medium grid mesh with a curvature refinement at the elbows as shown in Figure 12. The justification for this choice lies in capturing the secondary sloshing phenomenon as highlighted in Figure 13, in which the Refined Medium mesh reaches a slightly better accuracy in describing the motion of the secondary wave and the free-surface compared to the homologous case in Figure 10a. The adopted combination resembles a good balance between the solution accuracy and the computational cost. About this last point, the computational cost is not reported because the setups are difficult to compare. The number of CPUs (Intel Xeon Scalable Processors Gold 6130 2.10 GHz) used was defined as a function of the number of cells, and the trend of iterations over time does not scale linearly with the number of cores. The simulations generally settled on a negligible memory cost, about 2 GB of RAM per million cells.

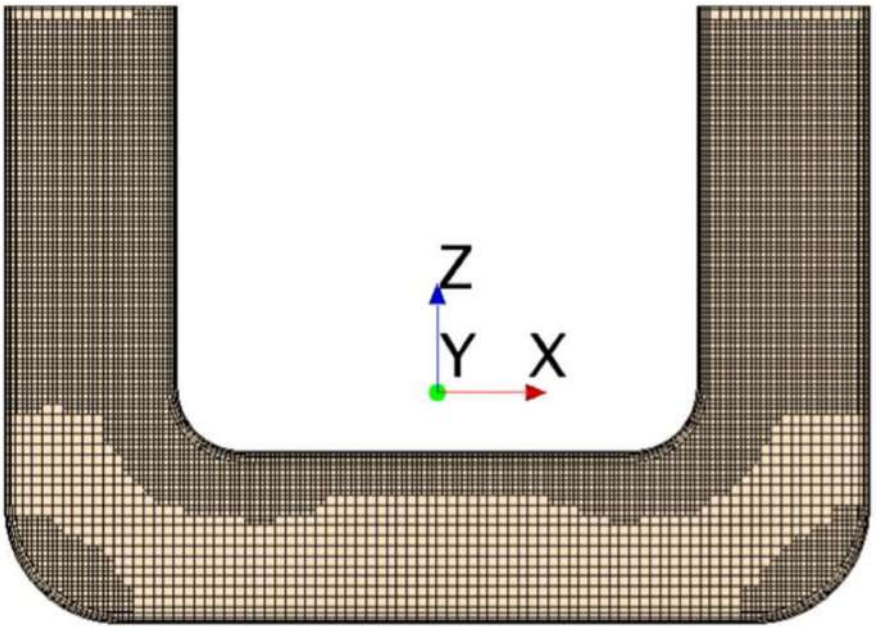

Figure 12. Refined Medium grid setup adopted.

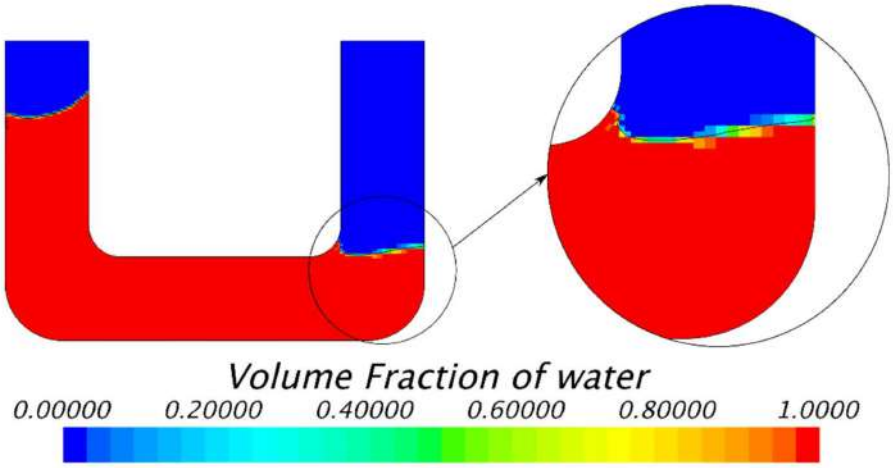

Figure 13. Volume of water and secondary wave of the Refined Medium mesh.

4. Results

In this section, we present the regular wave analysis outcomes, which serve as the foundational investigation for validating and verifying the results against experimental data. Once the fidelity of the CFD simulations is demonstrated in comparison to the experimental findings, we examine and compare the lumped parameter model outlined in Equation (5).

Subsequently, our analysis shifts its focus to the study of irregular waves, where we demonstrate the efficacy of the linear model with the results obtained via CFD numerical simulations.

4.1. Regular Motion Analysis and Validation of the CFD Setup

First, the results are presented in the regular harmonic rotation analysis, starting from the numerical outcomes of the CFD simulations imposing the angular motion:

$$\delta = A \sin\left(\frac{2\pi}{T} t\right) \tag{13}$$

Throughout this study, we maintained a constant amplitude (A), while systematically altering the period (T) within a range spanning from 1.1 to 1.8 s. As shown in time histories of the water angle $\tau(t)$ in Figure 14 (reduced to seven examples from 1.1 to 1.6 s of the period of Equation (13)), it was observed that the resonant period of the scaled device, as determined via both simulation and physical testing, converged to $T = 1.4$ s.

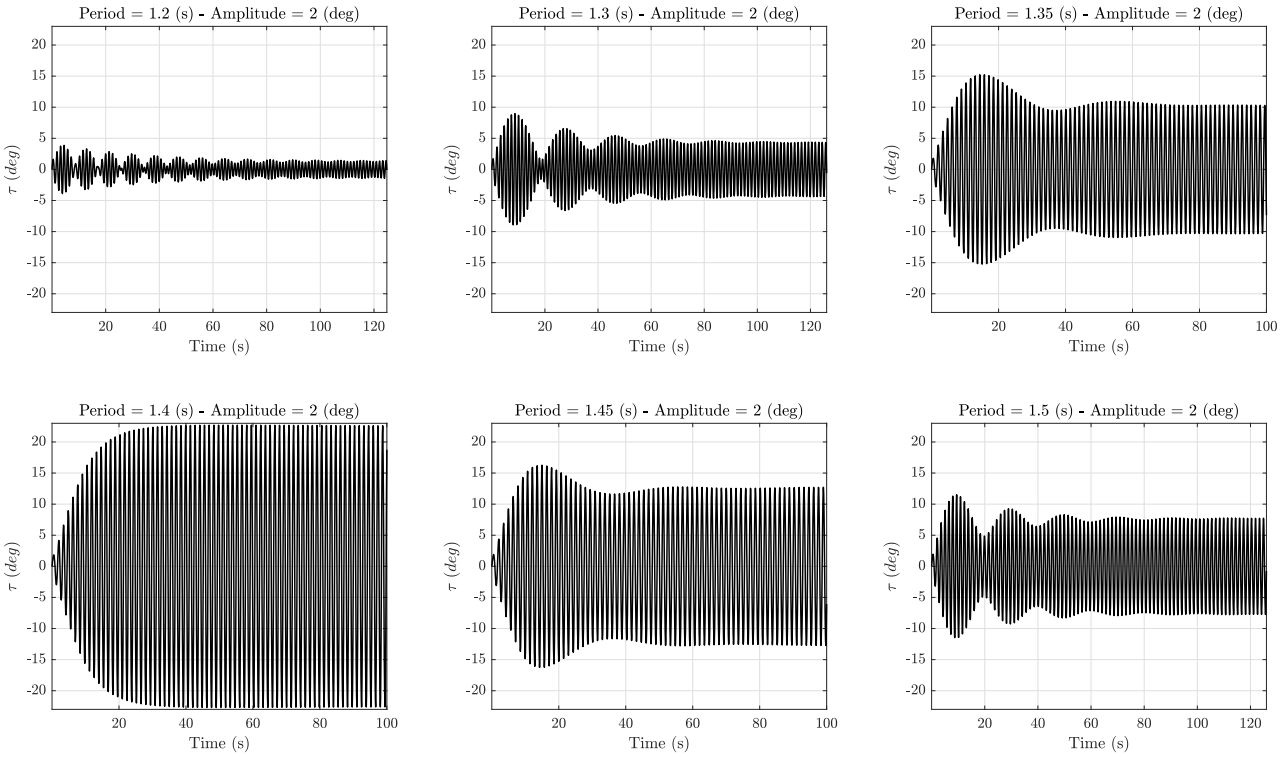

Figure 14. Water angle time history $\tau(t)$ of the CFD simulations with time step $dt = 0.5$ ms.

Amplitude assessments were performed by utilizing the Fast Fourier Transform (FFT) technique, and the resultant amplitudes, which were fitted using a cubic Hermite interpolant, were rigorously compared against the corresponding experimental data, as depicted in Figure 15. Notably, simulations employing finer time steps exhibited closer alignment with the experimental outcomes, albeit at the expense of a threefold increase in computational time. Consequently, we limited the number of simulations conducted under the resonance condition to optimize computational efficiency.

Observing the relative percentage error plot in Figure 16, the CFD setups exhibit limitations in accurately capturing the subtle water oscillations at the two lowest periods, resulting in relatively high error percentages. Additionally, during these periods, the amplitude of water level oscillation is either equal to or smaller than the size of the computational cells where the free surface is located. On the contrary, the CFD setups effectively capture water oscillations at the two highest periods ($T = 1.7$ s and $T = 1.8$ s). While still relatively subtle, these oscillations are more pronounced than those observed at the lowest two periods. At the resonant period ($T = 1.4$ s), the CFD simulations with $dt = 0.5$ ms achieve a relative error with respect to the corresponding experimental results of -6.99%. However, as we approach periods close to the maximum, accuracy diminishes. This decrease in accuracy can be attributed to limitations in the experimental setup's precision in setting the motion period with high precision. Consequently, errors become more pronounced where the curve exhibits steeper slopes. For instance, if the value corresponding to the period $T = 1.3$ s is, in reality, closer to $T = 1.28$ s, due to limitations in the experimental setup's precision, the disparity between the experimental value and the CFD result becomes more significant.

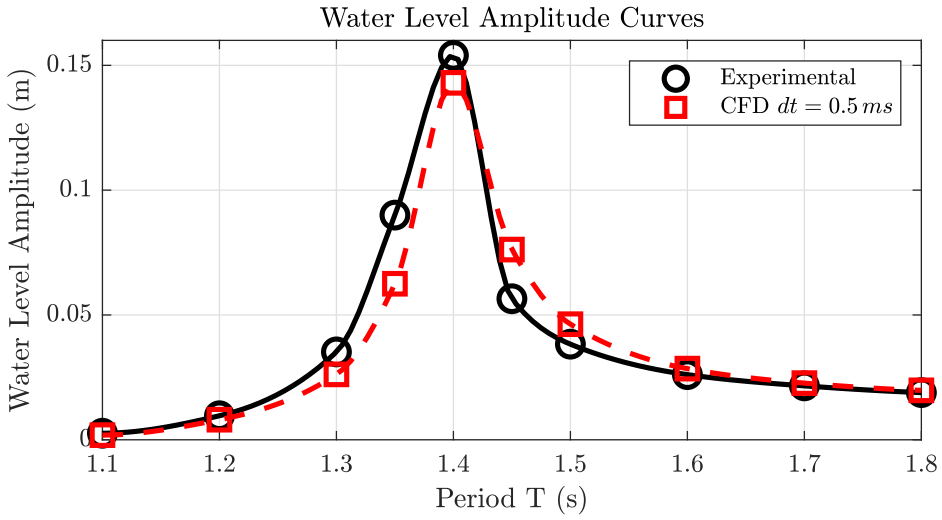

Figure 15. Water level amplitude comparison between experimental data and CFD results in regular wave analysis over input period T.

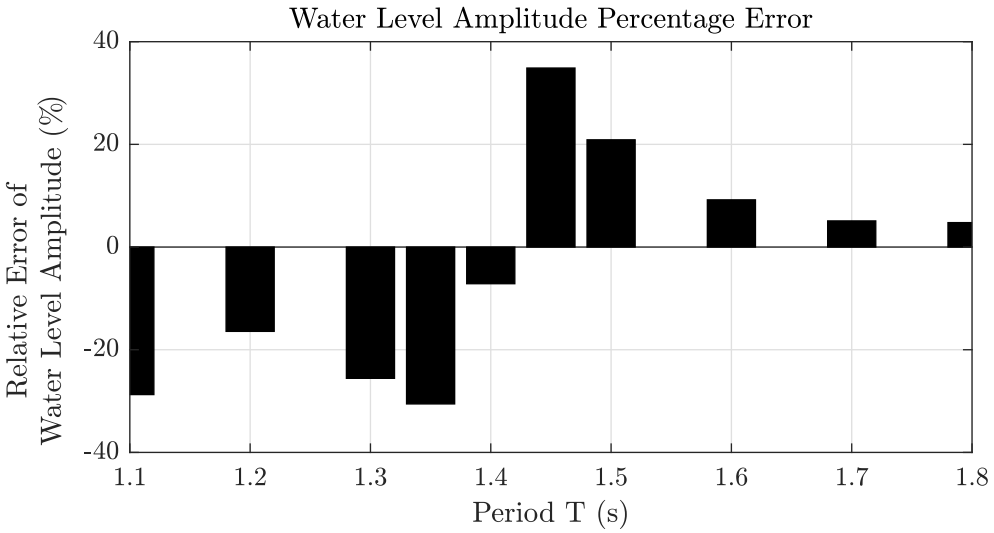

Figure 16. Relative error of the water level amplitude with respect to the experiments.

4.2. Tuning of the Linear Model

The U-tank device is most frequently employed in naval and marine settings, encompassing various applications. To effectively simulate and analyze such systems, subject to irregular input conditions, it is preferable to draw upon linear models better suited for rapid and preliminary responses in design stages. In this chapter, the lumped parameter model in Equation (5) is enhanced via experimental free-decay tests of the U-tank. The tuned model is described by the following Equation (14), in which the calibration is made on the inertial term via the mass coefficient K in Equation (15), and the damping term $b^*_{\tau\tau}$ in Equation (16), by means of the damping term q in Equation (17):

$$Ka_{\tau\tau}\ddot{\tau} + b^*_{\tau\tau}q\dot{\tau} + c_{\tau\tau}\tau = 0 \tag{14}$$

$$K = \frac{c_{\tau\tau}}{a_{\tau\tau}}\frac{1}{\omega_n} \tag{15}$$

$$b^*_{\tau\tau} = Q_t w_r I_2 \tag{16}$$

$$q = 2\xi\omega_n \frac{Ka_{\tau\tau}}{b^*_{\tau\tau}} \tag{17}$$

The time-domain free-decay model of the U-tank system can be expressed by the classical expression of a second-order system:

$$\ddot{\tau} + 2\xi\omega_n\dot{\tau} + \omega_n^2\tau = 0 \tag{18}$$

whose solution can be obtained by integrating in time:

$$\tau = \tau_0 e^{-\xi\omega_n} \sin\left(\omega_n\sqrt{(1-\xi^2)}t + \phi\right) \tag{19}$$

The computation of the natural frequency ω_n and the damping coefficient ξ is performed by means of the validated CFD simulation of a free-decay test. Then, the water angle signal over time is approximated via the least squares method with the following approximation function:

$$f = Ae^{-bt}\sin(\omega t + \phi) \tag{20}$$

The experimental data are fitted as shown in Figure 17 and the fitting parameters, as well as the tuning coefficients of the water angle, by comparison of Equations (19) and (20), are shown in Table 5.

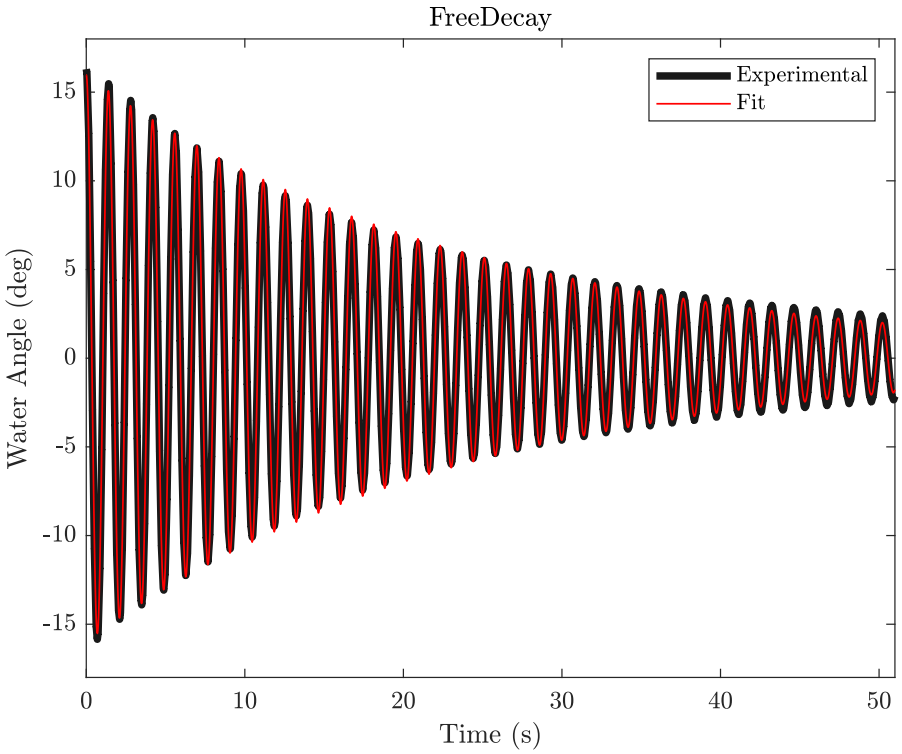

Figure 17. Free-decay test of the U-tank model and fitting (red-line) by means of Equation (20).

Table 5. Fitting coefficients of Equations (20) and (19) and goodness of fit of the free-decay simulation in Figure 17 and tuning parameters of enhanced model in Equation (14).

Parameter	Symbol	Value	Units
Coefficient of Determination	R^2	0.998	-
Root-Mean-Square Error	RMSE	0.192	deg
Initial Value	τ_0	15.97	deg
Damping Ratio	ξ	0.0091	-
Natural frequency	ω_n	4.526	rad/s
Mass Correction	K	0.830	-
Damping Factor	q	0.0117	m/s

The tuned outcomes are presented in the regular wave analysis about the Response Amplitude Operator (τ/δ), as illustrated in Figure 18. This operator signifies the relationship between the amplitudes of the water angle and the input parameter δ for the applied rotational amplitude $A = 2\,\text{deg}$, as defined in Equation (13).

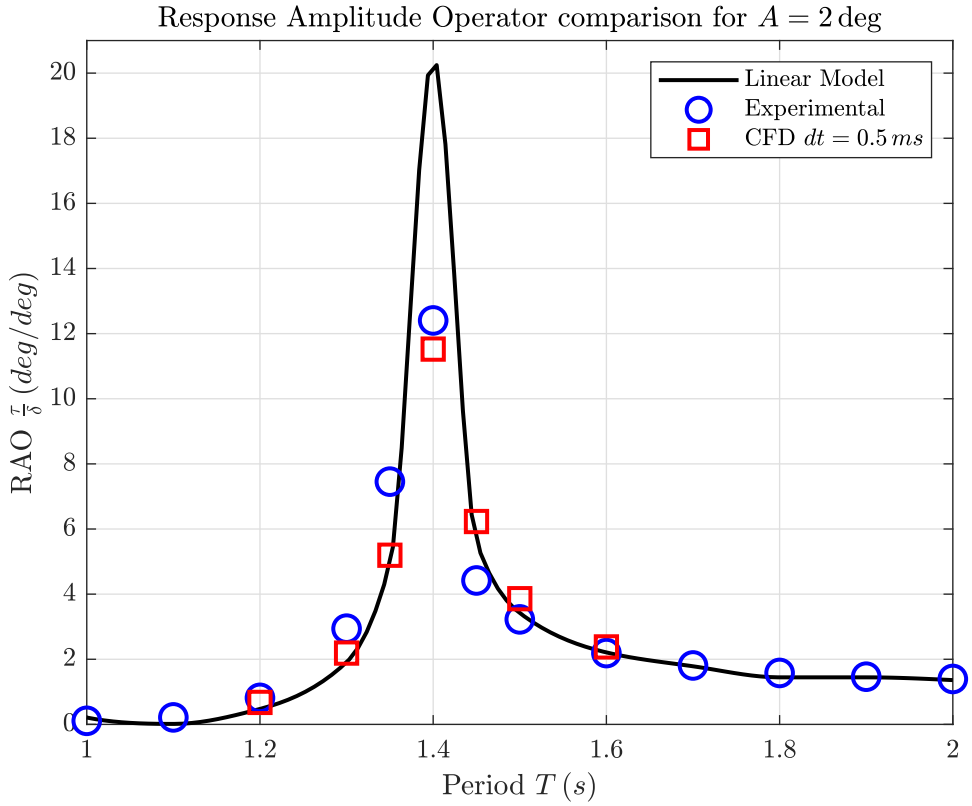

Figure 18. Response Amplitude Operator of the water angle and comparison between the Linear Model in Equation (5), experimental data, and CFD simulation.

In Figure 18, we compare the outcomes obtained from three sources: the linear-tuned model expressed in Equation (14), the experimental data, and the CFD simulations. The results from the numerical simulations exhibit a commendable level of agreement with the experimental data.

Nevertheless, it is worth highlighting that CFD numerical simulations effectively capture the dynamics of the U-tank, rendering them a valuable tool for fine tuning and calibrating the lumped parameter model derived from Lloyd in Equation (5).

4.3. Irregular Motion Analysis

The device's dynamics behavior is studied in irregular motion analysis starting from the spectra definition of the JONSWAP formulation [21], which is suitable and commonly used in the marine field for seas with limited fetch [22]. Within this formulation, the energetic content of an irregular sea is represented by the following spectral density function in Equation (21), defined by a significant wave height H_s , which is an average measurement of the highest third of waves and also related to the zero-order moment of the spectrum and the peak period T_p (or angular frequency ω_p, i.e., the wave period associated with the most energetic waves).

$$S(\omega) = A\omega^{-5}\exp\left(-B\omega^{-4}\right)\gamma^{\alpha} \tag{21}$$

In which, $A = A(H_s, T_p)$, $B = B(T_p)$, and, $\alpha = \alpha(\omega, T_p)$, can be found in the literature [21]. In this analysis, a single spectrum is studied by considering the root-mean-square value of the input signal $\delta_{RMS} = 1.5\,\text{deg}$, so the significant wave height is defined as

$H_s = 4\delta_{RMS}$. The spectrum is centered in the U-tank resonance condition ($T_p = 1.4$ s). Once the spectrum of the rotational motion S_δ is defined, it is possible to generate an associated time history, which is the input of the CFD simulation; both the spectrum and the time history are shown in Figure 19 and Figure 20, respectively.

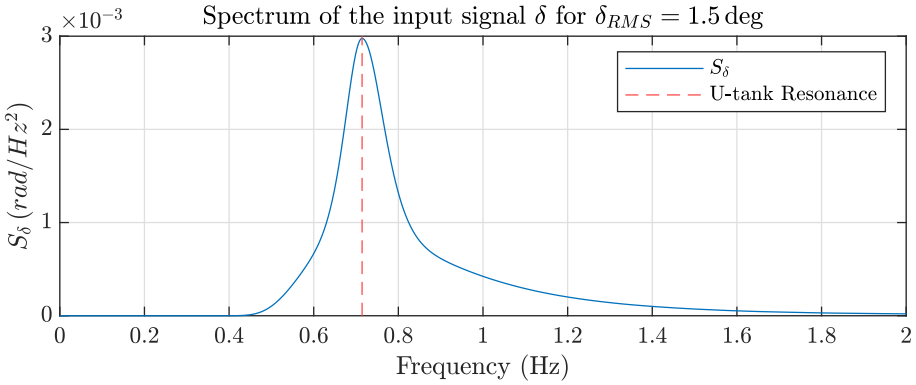

Figure 19. Jonswap spectrum of rotation δ for irregular input used in the time-domain irregular wave analysis.

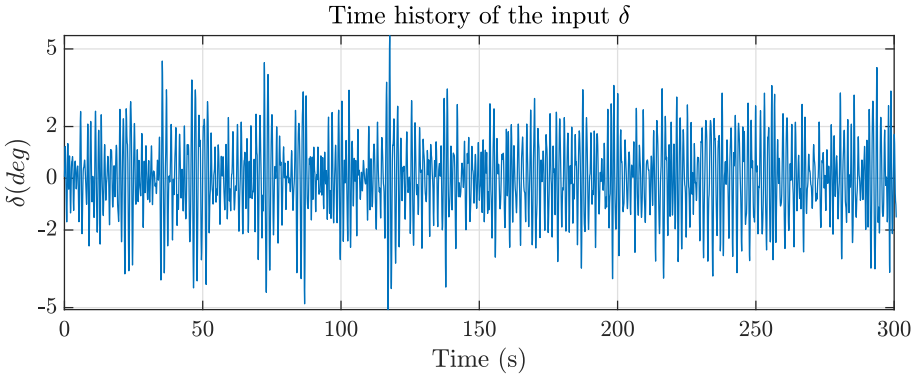

Figure 20. Time history of the pitch δ signal used in the time-domain irregular wave analysis and derived from the JONSWAP spectrum in Figure 19.

The tuned model is compared with validated CFD simulations as detailed in the following figure, Figure 21.

In this analysis, the torque, due the U-tank water dynamic, is also investigated and computed numerically from CFD as a direct outcome from the resolution of the fluid-dynamics equation, as well as analytically from the formulation in Equation (5) as:

$$M_\tau = a_{5\tau}\ddot{\tau} + c_{5\tau}\tau \tag{22}$$

The torque results in the time domain are reported in Figure 22 analogously to the water angle shown above.

The well capturing of the frequencies are estimated via the Welch's power spectral density of the time-domain signals, both of the water angle τ and the torque M_τ, as illustrated in Figure 23.

The quantitative comparison between the linear model and the CFD simulation, both in terms of water angle and torque, is summarized in Table 6 and shows a better estimation of the water angle τ than the torque M_τ.

The linear model overestimates the water angle, although within an acceptable discrepancy of around 3%. On the other hand, concerning the rms torque, there is a perfect overlap of the values with a relative difference between the linear model and CFD (a reference for the above validation) of less than one one-hundredth of a percent.

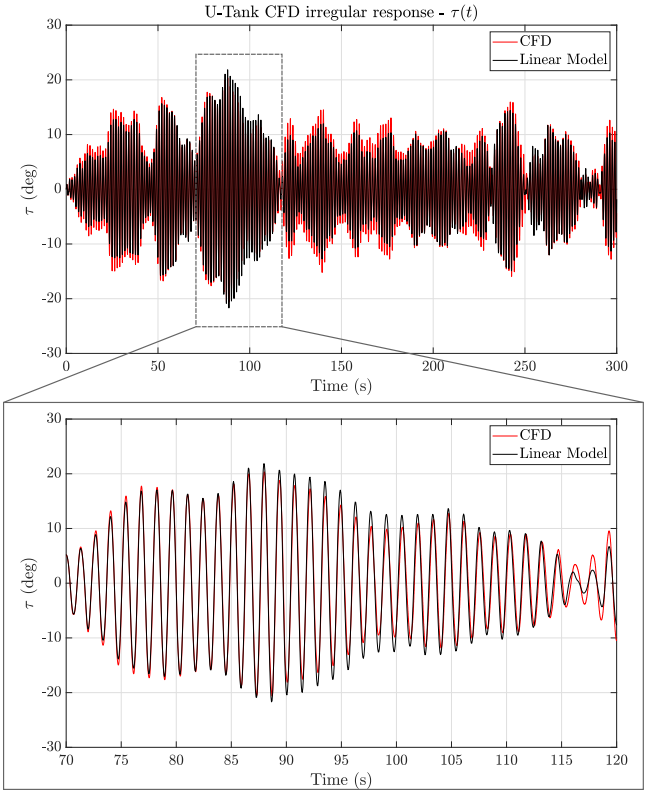

Figure 21. Water level over time in the CFD simulation and linear model (**top**), with magnification in a relevant interval (**bottom plot**).

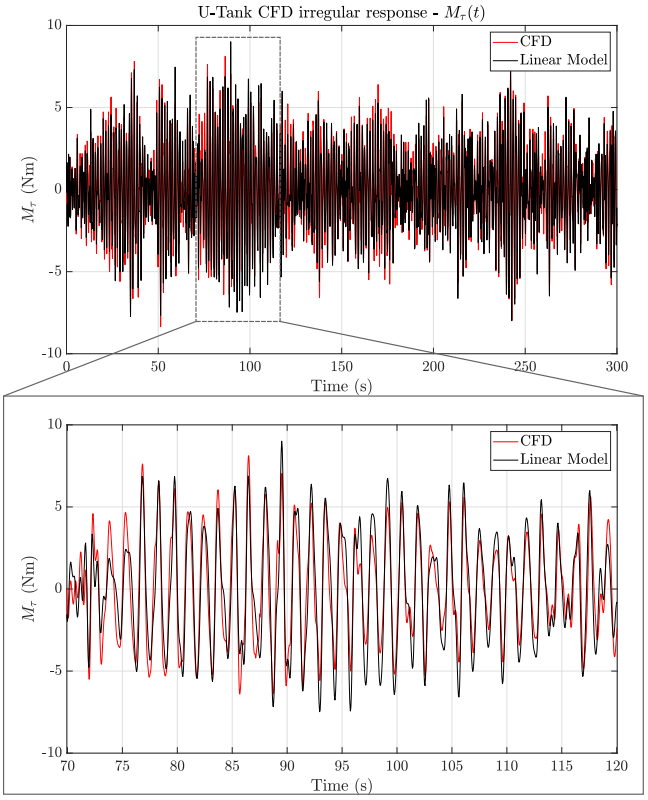

Figure 22. U-tank torque over time in the CFD simulation and linear model (**top**), with magnification in a relevant interval (**bottom plot**).

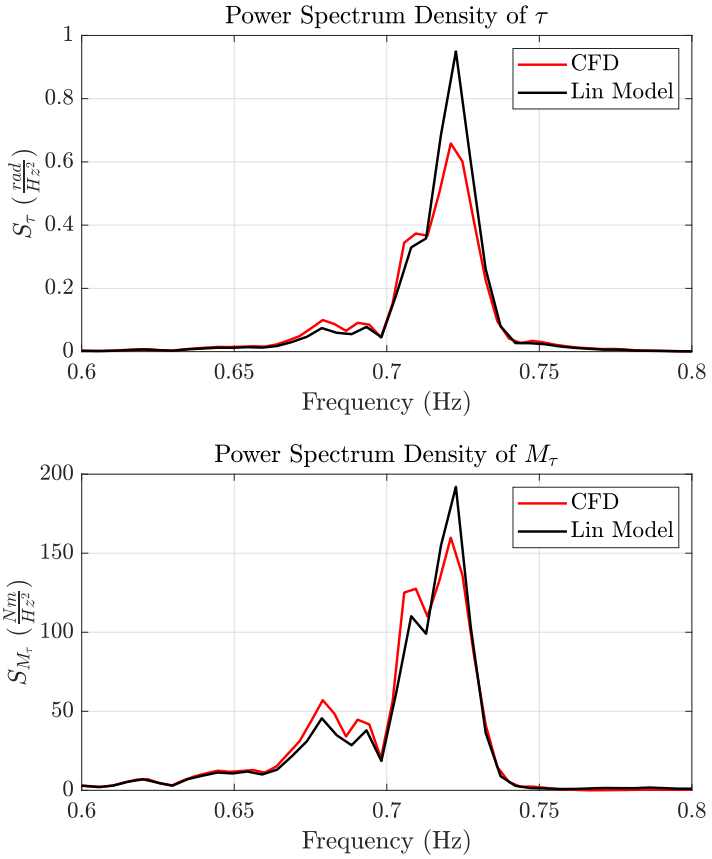

Figure 23. PSD comparison of CFD and Linear Lumped Parameter Model of water spectra (**top**) and torque (**bottom**).

Table 6. Comparison of RMS Values of water angle τ and U-tank torque M_τ. The relative difference of the linear model in Equation (14) is computed with respect to the validated CFD model

RMS	CFD	Linear Model	Rel. Difference (%)
τ (deg)	7.295	7.543	+3.39%
M_τ (Nm)	2.538	2.545	+0.26%

5. Coupling with Wave Energy Converter and Performance Enhancement

The U-shaped sloshing tank, as described and examined in this study, is seamlessly integrated into a pitching Wave Energy Converter (WEC) to enhance its operational bandwidth, consequently elevating its overall performance. The WEC under consideration here is the PEndulum WEC [23–25], a self-referenced inertial-based floating WEC consisting of an enclosed hull that houses a pendulum and the power take-off (PTO) system. The device is based on matching its resonance condition and the period of the incoming wave to harness energy. The device's schematic representation is presented in Figure 24. As the device reacts to motion induced by the waves, a relative displacement arises between the hull and the internal pendulum, with pitching motion playing a primary role. The kinetic energy associated with this relative motion is efficiently converted into electrical energy by the PTO system, which is directly linked to the pendulum's pivot point.

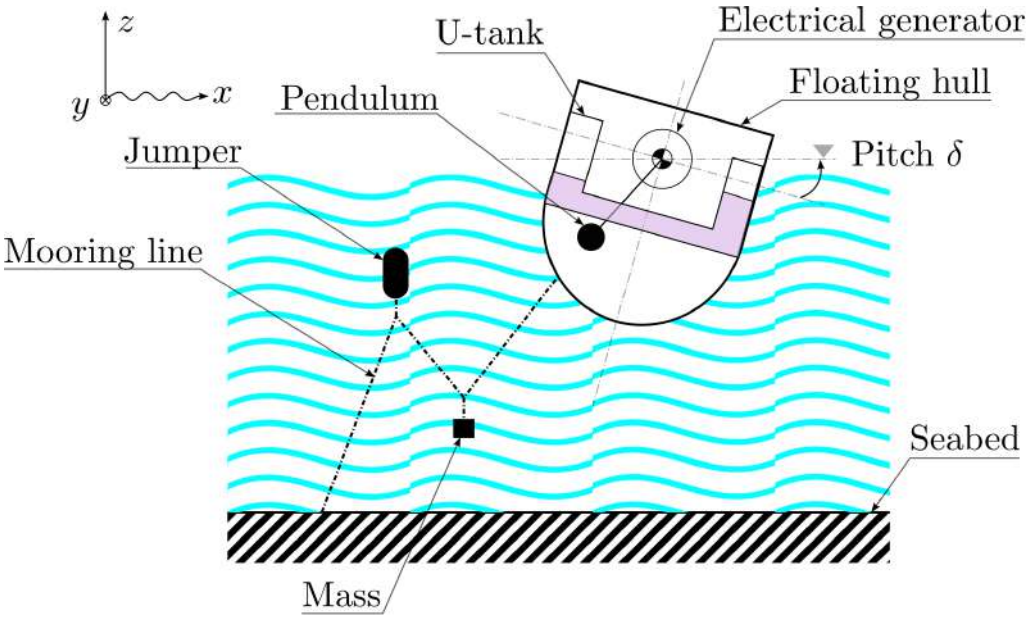

Figure 24. PeWEC scheme with enclosed U-tank device.

The properties of the PeWEC device from [26] are shown in Table 7.

Table 7. PeWEC configuration and geometrical properties.

Quantity	Value	Unit
Length (x-axis [1])	14.8	m
Width (y-axis)	22.5	m
Draft	4.81	m
Volume	1601	m^3
Pendulum mass	93	t
Generator rated power	523	kW
Ballast mass on the hull	803	t
Hull mass	222	t

[1] Direction of the incoming waves.

A suitable and feasible U-tank device has been preliminarily identified for the given PeWEC case, taking into consideration the following factors:

- The U-tank's mass is 15% of the total WEC mass;
- The overall mass is maintained at a constant level to ensure a consistent draft and, consequently, to preserve the hydrostatic stiffness of the entire system. Consequently, any additional mass resulting from integrating the U-tank is compensated for by adjusting the ballast;
- The combination of U-tank integration and ballast removal is guided by the constraint of keeping the device's Center of Gravity (CoG) in its original position;
- Two U-tank devices are positioned on the starboard and port sides. In this one-dimensional analysis, focusing solely on pitch motion (δ), they are represented as an equivalent U-tank device.
- The design of the U-tank device aims to broaden its operational bandwidth to accommodate longer incoming waves. Thus, the U-tank device is engineered to have a more extended resonance period than the WEC, which is designed for the Mediterranean Sea (for additional details, refer to [27]). The target resonance period for the WEC is approximately 6 s. Accordingly, the resonance of the U-tank is determined by

the definition of the natural period of the typical second-order system expressed in Equation (14):

$$T_n = 2\pi\sqrt{\frac{Ka_{\tau\tau}}{c_{\tau\tau}}} \tag{23}$$

In light of this, the presented U-tank case is designed with the characteristics in Table 8 and enclosed in the PeWEC device according to the scheme in Figure 25. It is pointed out that the U-tank devices are placed at the starboard and port side of the WEC; this effect is taken into account by considering an equivalent device with the depth $x_{t_{eq}}$ (two times the depth of the single tank).

Table 8. Geometrical characteristics of U-tank integrated in PeWEC device.

Size	Symbol	Value	Unit
CoR Distance	r_d	0.686	m
Duct Height	h_d	0.867	m
Duct Width	w_d	6.392	m
Reservoir Width	w_r	2.482	m
Total Height	H	4.740	m
Equivalent Depth	$x_{t_{eq}}$	12.3	m
Water (Datum) Level	h_r	1.566	m
Mass	$m_{\text{U-tank}}$	137.7	tons
Resonance Period	T_{res}	11.2	s

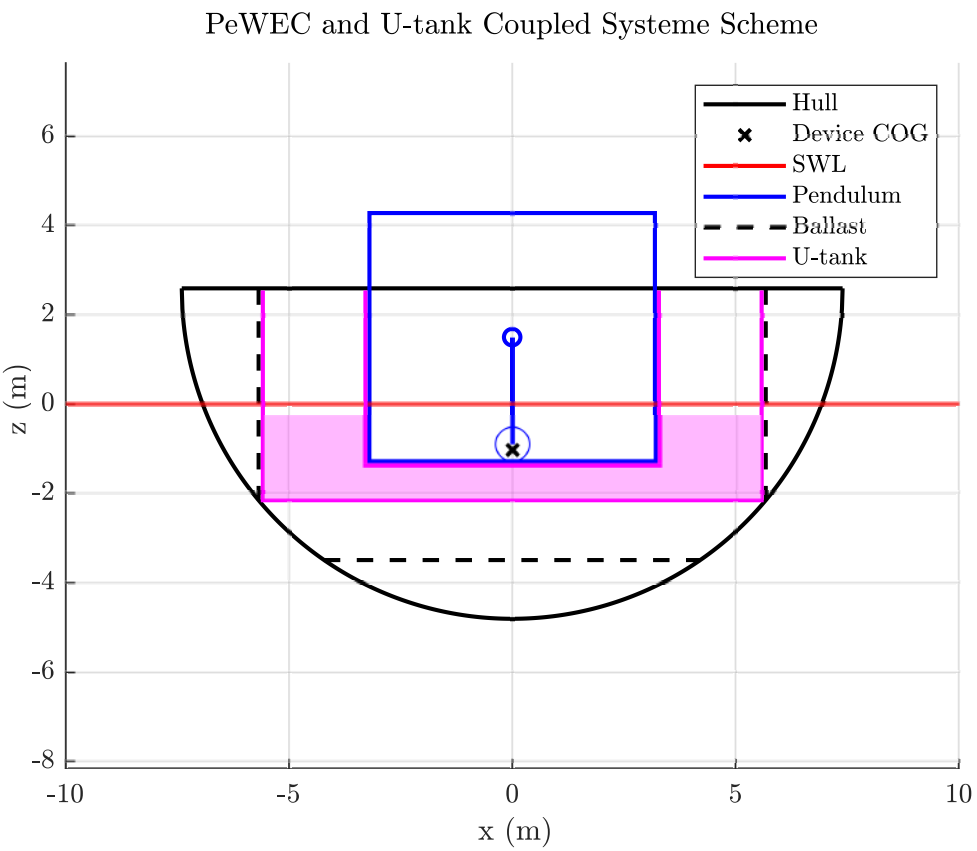

Figure 25. PeWEC scheme with enclosed U-tank device. The scheme is centered on the Sea Water Line (SWL).

The hydrodynamic behavior of the PeWEC device can be described by Cummins' equation in the time domain:

$$(\mathbf{M} + \mathbf{A}_\infty)\{\ddot{X}\} + \int_{-\infty}^{t} \left[h_r\left(t - t'\right)\right]\{\dot{X}\}dt' + \mathbf{K}\{X\} = \{F_w(t)\} \tag{24}$$

Remark 1. *The column vectors are notated between graph brackets.*

Remark 2. *The matrices are in bold characters.*

Remark 3. *$\dot{x}$ indicates the time derivative $\frac{\partial x}{\partial t}$.*

Equation (24) contains the mass matrix of the floater **M**, the added mass $\mathbf{A}_\infty$ evaluated at infinite oscillation frequency ω, the argument of the convolution integral is the impulse response function of the radiation forces, the hydrostatic stiffness **K**, and the wave forces vector $\{F_w(t)\}$ [28]. Through Olgivie's relations [29], the added mass and the radiation damping can be calculated as follows:

$$\mathcal{A}(\omega) = A_\infty - \frac{1}{\omega}\int_{\mathcal{R}^+} h_r(\tau)\sin(\omega t)d\tau \tag{25}$$

$$\mathcal{B}(\omega) = \frac{1}{\omega}\int_{\mathcal{R}^+} h_r(\tau)\cos(\omega t)d\tau \tag{26}$$

The added mass in Equation (25) and the radiation damping in Equation (26) are calculated via Boundary Element Method (BEM) codes such as NEMOH [30]. The equation of motion becomes

$$-\omega^2[\mathbf{M} + \mathcal{A}(\omega)]\{X\} + i\omega\mathcal{B}(\omega)\{X\} + K\{X\} = \{F_w(i\omega)\} \tag{27}$$

The array $\{X\} \in \mathbb{R}^{n\times 1}$, where n is the number of the degrees of freedom of the system; in general, it contains the six spatial motions, the proper PeWEC DoF (the pendulum angle ε), and the U-tank water angle (τ).

$$\begin{aligned}\{X\}^T &= \{x, y, z, \phi, \delta, \psi\, \varepsilon, \tau\} = \\ &= \{\text{surge}, \text{sway}, \text{heave}, \text{roll}, \text{pitch}, \text{yaw}, \text{pendulum}, \text{U-tank}\}\end{aligned}$$

Within the purview of this research, the Power Take-Off system (PTO) is disabled to study the influence of the U-tank on the pitch angle only (5th DoF, considering the notation in Equation (5)). Indeed, the complete system is reduced to the heave-pitch coupling and the integration of the U-tank:

$$\{X\}^T = \{z, \delta, \tau\}$$

and the equation of motion is coupled with the U-tank dynamics in Equation (5).

The dynamic response of the system under regular waves with frequency ω and unitary amplitude is described via the Response Amplitude Operator (RAO) defined as

$$RAO(\omega) = \frac{f_w(\omega)}{-\omega^2[\mathbf{M} + \mathcal{A}(\omega)] + i\omega\mathcal{B}(\omega) + K} \tag{28}$$

To be noted that RAO is normalized on the amplitude A_w on the wave forces $F(i\omega) = A_w f_w(i\omega)$. The results are depicted in Figure 26, where a comparison is made between the pitch angles (δ) of the PeWEC-only system and the Coupled System. The pitch angles are presented on the right-axis, while the left-axis displays the U-tank water angle RAO. It is important to note that while the maximum amplitude of the pitch motion is reduced compared to the original case, a secondary peak emerges at more extended periods, expanding the system's capabilities beyond its initial configuration. In fact, the goal set in this work is

achieved with the addition of the second peak, making the device work at longer periods (associated with higher waves) where it was previously ineffective. On the other hand, an anti-resonance occurs at the U-tank resonance period of 11.2 s, as reported in Table 8.

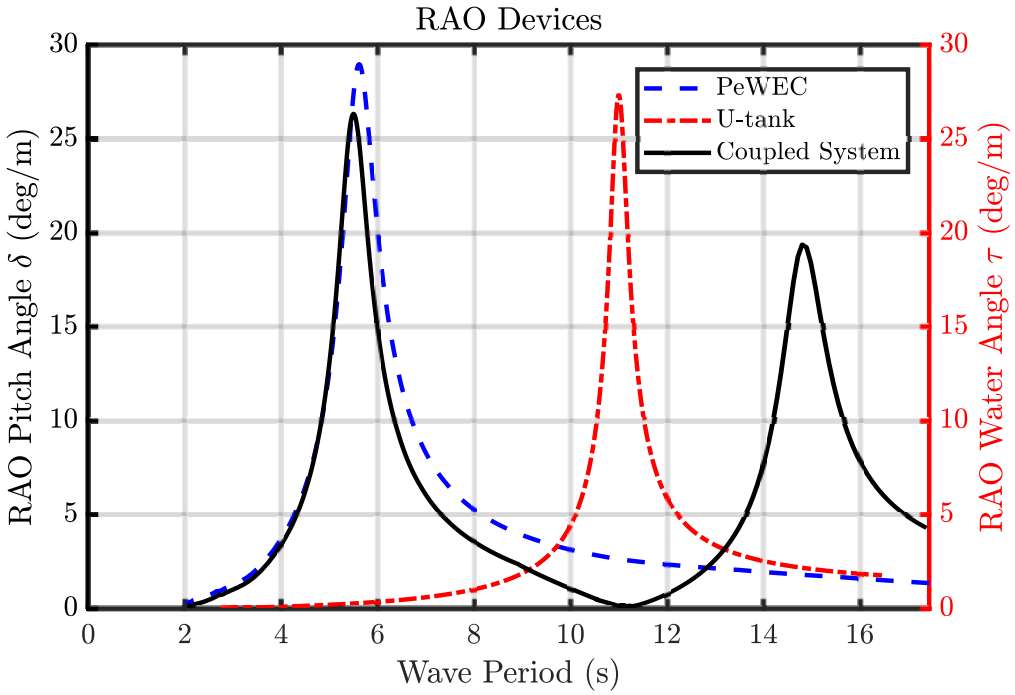

Figure 26. RAO of the pitch angle δ of the PeWEC and Coupled Device (left black y-axis) and U-tank water angle τ (right red y-axis) over the incoming wave period. The dashed blue line indicates the WEC-only system, the dashed red line indicates the U-tank device, and the continuous black line indicates the Coupled System PeWEC and U-tank.

6. Conclusions

In summary, this paper has comprehensively investigated a U-shaped sloshing tank. The study employed a linear model compared to a numerical simulation conducted via Computational Fluid Dynamics (CFD) techniques. Notably, the validity of the CFD approach was rigorously established via experimental tests, in which motion was imposed using an electro-actuated motion platform. Subsequently, the CFD methodology was corroborated and refined based on the insights gained from these experimental results. As a result, the linear lumped parameter model was enhanced with the input derived from the CFD simulations, advancing our understanding of the U-shaped sloshing tank dynamics.

The refined linear model demonstrated a remarkable level of agreement with the rigorously validated numerical results. This enhanced model offers a reliable tool for advanced preliminary research endeavors, particularly the intricate coupling of the sloshing tank with floaters in marine applications. Moreover, it paves the way for implementing precise control strategies for diverse purposes. The results presented in this study underscore the model's capacity for accuracy and highlight its adaptability, indicating its suitability for a wide range of future applications without compromising precision, thanks to the improvements showcased herein.

In conclusion, the integration of the U-tank device with a pitch-based wave energy converter is demonstrated and the results indicate a notable improvement in the WEC's performance over more extended periods, where it previously faced limitations in its efficiency. A reduction of approximately 8.6% in pitch amplitude was observed. However, it is crucial to emphasize that, concurrently with this reduction, a remarkable peak arises in a longer period, when the WEC was originally inactive, resulting in an 850% increase in pitch amplitude. This enhancement represents a significant step towards optimizing the system's

capabilities for longer wave cycles, underscoring its practical value. A detailed analysis of this phenomenon will require further research to fully understand the integration of the U-shaped tank with an oscillating WEC, especially concerning control strategies to address this second peak during the operational phases of the device through tuning interventions.

Author Contributions: Conceptualization, M.F., M.A. and S.A.S.; methodology, G.G. and E.G.; software, M.F. and M.A.; validation, M.F., M.A. and S.B.; formal analysis, M.F.; investigation, M.F. and M.A.; resources, M.F.; data curation, M.F.; writing—original draft preparation, M.F.; writing—review and editing, M.F. and G.G.; visualization, M.F. and M.A.; supervision, S.A.S.; project administration, S.A.S.; funding acquisition, G.G. and S.A.S. All authors have read and agreed to the published version of the manuscript.

Funding: This research received no external funding.

Institutional Review Board Statement: Not applicable.

Informed Consent Statement: Not applicable.

Data Availability Statement: Data is contained within the article.

Acknowledgments: Computational resources were provided by HPC@POLITO, a project of Academic Computing within the Department of Control and Computer Engineering at the Politecnico di Torino (http://www.hpc.polito.it, accessed on 1 September 2023).

Conflicts of Interest: The authors declare no conflict of interest.

References

1. Froude, W. *On the Rolling of Ships. Read at the Second Session of the Institution of Naval Architects, and Repr. from the Transactions*; Parker, Son, and Bourn: London, UK, 1862.
2. Frahm, H.H. Results of trials of the anti-rolling tanks at sea. *J. Am. Soc. Nav. Eng.* **1911**, *23*, 571–597.
3. Minorsky, N. Problems of anti-rolling stabilization of ships by the activated tank method. *J. Am. Soc. Nav. Eng.* **1935**, *47*, 87–119.
4. Chadwick, J.; Klotter, K. On the dynamics of anti-roll tanks. *Schiffstechnik* **1954**, *2*, 23–45.
5. Van Den Bosch, J.; Vugts, J. *Roll Damping by Free Surface Tanks*; TNO-Report; TU Delft: Delft, The Netherland, 1966.
6. Stigter, C. The performance of U-tanks as a passive anti-rolling device. *Int. Shipbuild. Prog.* **1966**, *13*, 249–275.
7. Field, S.B.; Martin, J.P. Comparative Effects of U-Tube and Free Surface Type Passive Roll Stabilisation Systems. *Sci. Eng. Med. Naval Architect* **1975**, 73–92. Available online: https://api.semanticscholar.org/CorpusID:107310574 (accessed on 1 May 2021).
8. Webster, W.; Dalzell, J.; Barr, R. Prediction and measurement of the performance of free-flooding ship antirolling tanks. *Soc. Nav. Archit. Mar. Eng.-Trans.* **1988**, *96*, 32.
9. Lee, B.; Vassaols, D. An investigation into the stabilisation effects of anti-roll tanks with flow obstructions. *Int. Shipbuild. Prog.* **1995**, *43*, 70–88.
10. Gawad, A.F.A.; Ragab, S.A.; Nayfeh, A.H.; Mook, D.T. Roll stabilization by anti-roll passive tanks. *Ocean Eng.* **2001**, *28*, 457–469.
11. Lloyd, A. *Seakeeping: Ship Behaviour in Rough Weather*; Ellis Horwood Ltd.: Herts, UK, 1989; ISBN 0 7458 0230 3.
12. Zhong, Z.; Falzarano, M.; Fithen, R.M. A numerical study of U-tube passive anti-rolling tanks. In Proceedings of the ISOPE International Ocean and Polar Engineering Conference, Montreal, QC, Canada, 24–29 May 1998.
13. Van Daalen, E.; Kleefsman, K.; Gerrits, J.; Luth, H.; Veldman, A. Anti Roll Tank Simulations with a Volume Of Fluid (VOF) based Navier-Stokes Solver. In Proceedings of the Twenty-Third Symposium on Naval Hydrodynamics, Val de Reuil, France, 17–22 September 2000; National Academy Press: Washington, DC, USA, 2001; pp. 457–473.
14. Taskar, B.U.; DasGupta, D.; Nagarajan, V.; Chakraborty, S.; Chatterjee, A.; Sha, O.P. CFD aided modelling of anti-rolling tanks towards more accurate ship dynamics. *Ocean Eng.* **2014**, *92*, 296–303.
15. Kerkvliet, M.; Vaz, G.; Carette, N.; Gunsing, M. Analysis of U-type anti-roll tank using URANS: Sensitivity and validation. In Proceedings of the ASME 2014 33rd International Conference on Ocean, Offshore and Arctic Engineering, San Francisco, CA, USA, 8–13 June 2014; Volume 45400, p. V002T08A031.
16. Faedo, N.; Giorgi, G.; Ringwood, J.; Mattiazzo, G. Optimal control of wave energy systems considering nonlinear Froude–Krylov effects: Control-oriented modelling and moment-based control. *Nonlinear Dyn.* **2022**, *109*, 1777–1804.
17. Giorgi, G. Embedding Parametric Resonance in a 2:1 Wave Energy Converter to Get a Broader Bandwidth. *Renew. Energy* 2023, *submitted*.
18. Fontana, M.; Casalone, P.; Sirigu, S.A.; Giorgi, G.; Bracco, G.; Mattiazzo, G. Viscous Damping Identification for a Wave Energy Converter Using CFD-URANS Simulations. *J. Mar. Sci. Eng.* **2020**, *8*, 355. https://doi.org/10.3390/jmse8050355.
19. Siemens Digital Industries Software. *Simcenter STAR-CCM+ User Guide*, v. 2021.1; Siemens: Munich, Germany, 2021.
20. Shih, T.H.; Liou, W.W.; Shabbir, A.; Yang, Z.; Zhu, J. A new k-e eddy viscosity model for high reynolds number turbulent flows. *Comput. Fluids* **1995**, *24*, 227–238. https://doi.org/10.1016/0045-7930(94)00032-T.

21. Hasselmann, K.; Barnett, T.P.; Bouws, E.; Carlson, H.; Cartwright, D.E.; Enke, K.; Ewing, J.; Gienapp, A.; Hasselmann, D.; Kruseman, P.; et al. Measurements of wind-wave growth and swell decay during the Joint North Sea Wave Project (JONSWAP). *Ergaenzungsheft Dtsch. Hydrogr. Z. Reihe A* **1973**. Available online: https://hdl.handle.net/21.11116/0000-0007-DD46-2 (accessed on 1 November 2023).
22. Stansberg, C.; Contento, G.; Hong, S.W.; Irani, M.; Ishida, S.; Mercier, R.; Wang, Y.; Wolfram, J.; Chaplin, J.; Kriebel, D. The specialist committee on waves final report and recommendations to the 23rd ITTC. In Proceedings of the 23rd ITTC, Venice, Italy, 8–14 September 2002; Volume 2, pp. 505–551.
23. Carapellese, F.; Pasta, E.; Paduano, B.; Faedo, N.; Mattiazzo, G. Intuitive LTI energy-maximising control for multi-degree of freedom wave energy converters: The PeWEC case. *Ocean Eng.* **2022**, *256*, 111444. https://doi.org/10.1016/j.oceaneng.2022.111444.
24. Niosi, F.; Begovic, E.; Bertorello, C.; Rinauro, B.; Sannino, G.; Bonfanti, M.; Sirigu, S. Experimental validation of Orcaflex-based numerical models for the PEWEC device. *Ocean Eng.* **2023**, *281*, 114963. https://doi.org/10.1016/j.oceaneng.2023.114963.
25. Pasta, E.; Carapellese, F.; Faedo, N.; Brandimarte, P. Data-driven control of wave energy systems using random forests and deep neural networks. *Appl. Ocean Res.* **2023**, *140*, 103749. https://doi.org/10.1016/j.apor.2023.103749.
26. Giglio, E.; Petracca, E.; Paduano, B.; Moscoloni, C.; Giorgi, G.; Sirigu, S.A. Estimating the Cost of Wave Energy Converters at an Early Design Stage: A Bottom-Up Approach. *Sustainability* **2023**, *15*, 6756. https://doi.org/10.3390/su15086756.
27. Mattiazzo, G. State of the art and perspectives of wave energy in the Mediterranean sea: Backstage of ISWEC. *Front. Energy Res.* **2019**, *7*, 114.
28. Giorgi, G.; Sirigu, S.; Bonfanti, M.; Bracco, G.; Mattiazzo, G. Fast nonlinear Froude–Krylov force calculation for prismatic floating platforms: A wave energy conversion application case. *J. Ocean Eng. Mar. Energy* **2021**, *7*, 439–457.
29. Ogilvie, T.F. Recent progress toward the understanding and prediction of ship motions. In Proceedings of the 5th Symposium on Naval Hydrodynamics, Bergen, Norway, 10–12 September 1964; David W. Taylor Model Basin: Washington DC, USA, 1964; pp. 3–80.
30. Babarit, A.; Delhommeau, G. Theoretical and numerical aspects of the open source BEM solver NEMOH. In Proceedings of the 11th European Wave and Tidal Energy Conference (EWTEC2015), Nantes, France, 6–11 September 2015.